



Microwave-assisted synthesis of fluorescent carbon dots from nanocellulose for dual-metal ion-sensor probe: Fe (III) and Mn (II)

Donghao Hu · Kuan-Hsuan Lin · Yinchao Xu · Mikio Kajiyama · Marcos A. Neves · Kazuyoshi Ogawa · Toshiharu Enomae

Received: 8 April 2021 / Accepted: 31 July 2021 / Published online: 17 August 2021
© The Author(s), under exclusive licence to Springer Nature B.V. 2021

Abstract A simple one-step microwave-assisted synthesis approach for preparing fluorescent carbon dots (CDs) with an average diameter of 7.86 nm from 2,2,6,6-tetramethylpiperidine-1-oxyl radical-mediated-oxidized cellulose nanofiber (TEMPO-CNF) and 4,7,10-Trioxa-1,13-tridecanediamine is reported in this study. The synthesized TEMPO-CDs exhibited excitation-dependent emission, with optimal excitation and emission wavelengths of 390 nm and 449 nm (bright blue ray), respectively. The fluorescence

properties of the synthesized TEMPO-CDs were successfully and selectively quenched by Fe^{3+} within seconds and by Mn^{2+} after 10 min. Thus, this phenomenon is further applicable to the development of a fluorescence-sensing system for the quantitative detection of Fe^{3+} and Mn^{2+} using the same CD probe; this is the first time such findings have been reported in the CD-related literature.

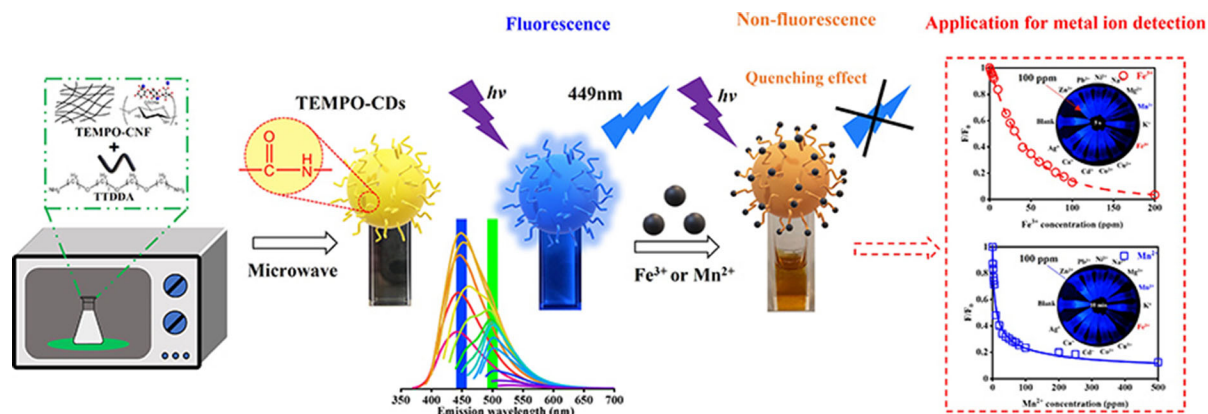
Supplementary Information The online version contains supplementary material available at <https://doi.org/10.1007/s10570-021-04126-9>.

D. Hu (✉) · K.-H. Lin
Graduate School of Life and Environmental Sciences,
University of Tsukuba, 1-1-1 Tennodai, Tsukuba,
Ibaraki 305-8577, Japan
e-mail: hudonghao@paperscience.org

Y. Xu
Key Laboratory of Recycling and Eco-treatment of Waste
Biomass of Zhejiang Province, Zhejiang University of
Science and Technology, Liuhe Rd, No. 318,
Hangzhou 310023, China

M. Kajiyama · M. A. Neves · K. Ogawa · T. Enomae
Faculty of Life and Environmental Sciences, University of
Tsukuba, 1-1-1 Tennodai, Tsukuba, Ibaraki 305-8577,
Japan

Graphic abstract



Keywords Carbon dots (CDs) · Nanocellulose · Microwave · Metal-ion detection

Introduction

Fluorescent nanoscale carbon particles were discovered by Xu et al. (2004) during the purification of carbon nanotubes; however, they were first given the name “carbon dots (CDs)” by Sun et al. (2006). Owing to their advantages of excellent photoluminescence, small-scale features (< 10 nm), low cytotoxicity, and ready surface functionalizability [compared with conventional semiconductor quantum dots (Baker and Baker 2010), CDs have excellent application prospects in the fields of environmental detection (Hu et al. 2014), biochemical sensing (Kiran and Misra 2015), photocatalysis (Li et al. 2010, 2013), electrocatalytic technologies (Tang et al. 2014), and elsewhere].

In recent years, several methods have been proposed for synthesizing CDs, including electric discharge, electrochemical oxidation, and thermal methods (Baker and Baker 2010). Among these methods, Zhu et al. (2009) reported a clean, cheap, and convenient microwave pyrolysis method. Meanwhile, various naturally occurring, environmentally friendly, cheap, and carbon-rich materials [e.g., food wastes (Park et al. 2014), goose feathers (Liu et al. 2015), and plant leaves (Li et al. 2013)] have been explored for conversion into CDs, to replace conventional sources [e.g., graphite (Li et al. 2010; Sun

2006), carbon nanoparticles (Li et al. 2011), petroleum coke (Wu et al. 2014), and chemicals such as L-ascorbic acid (Zhang et al. 2010), polyethylene glycol (Liu et al. 2011; Zhu et al. 2009), and citric acid (Li et al. 2014a)]. Nanocellulose (NC), produced from cellulose, is regarded as an inexhaustible natural biopolymer; it has been widely applied in printed electronics (Hoeng et al. 2016), biomedical applications (Jorfi and Foster 2015), packaging products (Hubbe et al. 2017), sensors (Golmohammadi et al. 2017), and optical materials (Kim 2015), owing to its excellent physical and chemical properties (Klemm et al. 2011).

As a result of rapid global industrialization, large quantities of metals have been excavated from the Earth’s crust, and several of them have been dispersed and accumulated in the pedosphere (Han et al. 2002; Singh et al. 2011). Heavy metal contamination has become a prominent environmental problem and risks undermining global sustainability through its various cytological and physiological effects (Duruibe et al. 2007).

Ferric ions (Fe³⁺) play an essential role in cytochromes and oxygen-binding molecules (Emerit et al. 2001). The toxicity of Fe³⁺ itself is not very high (WHO 2003); however, it can catalyze the generation of hydroxyl and organic free radicals; this makes it dangerous. Moreover, ferrous-ion (Fe²⁺) by-products accelerate free radical generation via direct oxygen interactions (Papanikolaou and Pantopoulos 2005). Free radicals pose a threat to important cellular macromolecules; they can cause injuries to the cardiovascular and nervous systems (Zarjou et al.

2011). Manganese (Mn) is essential for the proper development of brain functions, but Mn overexposure can have adverse effects on the health of several neurotransmitter systems, resulting in motor incoordination or emotional and cognitive dysfunction (Peres et al. 2016). The syndrome “manganism” occurs in response to high Mn exposure and is characterized by a “Parkinson-like syndrome,” including neurobehavioral manifestations, postural tremors, and rigid muscles (Racette 2014; WHO 2011). The risks of Mn contamination are not limited to metallic minerals but also to water and food with high Mn concentrations. Epidemiological studies have reported the adverse effects of excess Mn dissolved in drinking water (Kawamura et al. 1941; Yoshida and Yamada 1988; Kondakis et al. 1989).

To measure metal-ion concentrations, conventional assays [e.g., voltammetry, spectrophotometry, atomic absorption spectrometry, inductively coupled plasma mass spectrometry, and inductively coupled plasma optical (or atomic) emission spectrometry] are commonly used (Malik et al. 2019). However, these assays require sophisticated instrumentation, tedious sample-preparation procedures, and well-trained personnel; this makes their practical application difficult (Li et al. 2014b).

Recently, researchers have attempted to develop sensitive and inexpensive metal-sensing systems using novel physical, chemical, and biological methods. Among these attractive techniques, fluorescence (FL)-related optical approaches are regarded as a promising method for the detection of heavy metals, because they offer high specificity, low detection limits, fast response times, and technical simplicity (Chowdhury et al. 2018; De Acha et al. 2019; Wang et al. 2020). The optical properties of probes (e.g., absorption, FL intensity, and lifetime) can be varied through the binding and interactions of specific metals; this produces a quick response and suggests selective and sensitive functionality (Yoo et al. 2019).

CDs are desirable candidates for sensing metal ions because of their high stability, low toxicity, and low cost. Several fluorescent CD probes have been developed to detect metal ions (Sun and Lei 2017), including Ag^+ (Li et al. 2018; Zhu et al. 2014), Cd^{2+} (Xiao et al. 2019), Cu^{2+} (Wang et al. 2019; Yu et al. 2018b; Zong et al. 2014), Fe^{3+} (Li et al. 2014b; Liu et al. 2015; Yu et al. 2018a; Zhu et al. 2014), Hg^{2+} (Hou et al. 2015; Zhuo et al. 2017), Mn^{2+} (Yu et al.

2018b; Zhang et al. 2018), Pb^{2+} (Wang et al. 2019), and Zn^{2+} (Yang et al. 2018; Yu et al. 2018b). Among them, Fe^{3+} is one of the most frequently discussed species. Several of the related studies presented in Table S1 focus on the materials, methods, excitation and emission wavelengths, and detectable concentration ranges. Fluorescent CD probes for Mn^{2+} have been reported in fewer CD-related studies; Table S2 compares several of these against other fluorescent materials within an equivalent detection range.

In this study, we employed a simple and fast one-step microwave method for synthesizing fluorescent CDs from eco-friendly NC materials that are securely applicable to all environments. The synthesized TEMPO-CDs appeared yellow under daylight irradiation but blue under UV irradiation with excellent performance. In addition, by exploiting the quenching influence of metal ions on the disappearance of TEMPO-CD FL, the TEMPO-CD solution was applied as a sensor for both qualitative and quantitative detection of Fe^{3+} and Mn^{2+} . This is the first time to report a dual-metal ion-sensor probe for Fe^{3+} and Mn^{2+} among the CD-related applications. Compared to the detection methods via optical approaches for Fe^{3+} and Mn^{2+} metal ions in previous studies, the TEMPO-CD probe in this study showed a relative high sensitivity.

Materials

2,2,6,6-tetramethylpiperidine-1-oxyl radical-mediated-oxidized cellulose nanofiber (TEMPO-CNF) (1.08 wt% aqueous dispersion) was provided by Nippon Paper Industries Co., Ltd., Japan. Aqueous counter-collision cellulose nanofiber (ACC-CNF) (1.35 wt% aqueous dispersion) was obtained from Chuetsu Pulp & Paper Co., Ltd., Japan. Freeze-dried cellulose nanocrystal (CNC) powder, generated through the hydrolysis of softwood pulp with sulfuric acid, was purchased from the University of Maine, USA. Metal nitrate salts, including silver (AgNO_3), calcium [$\text{Ca}(\text{NO}_3)_2 \cdot 4\text{H}_2\text{O}$], cadmium [$\text{Cd}(\text{NO}_3)_2 \cdot 4\text{H}_2\text{O}$], cobalt [$\text{Co}(\text{NO}_3)_2 \cdot 6\text{H}_2\text{O}$], copper [$\text{Cu}(\text{NO}_3)_2 \cdot 3\text{H}_2\text{O}$], iron [$\text{Fe}(\text{NO}_3)_3 \cdot 9\text{H}_2\text{O}$], potassium (KNO_3), magnesium [$\text{Mg}(\text{NO}_3)_2 \cdot 6\text{H}_2\text{O}$], manganese [$\text{Mn}(\text{NO}_3)_2 \cdot 6\text{H}_2\text{O}$], sodium (NaNO_3), nickel [$\text{Ni}(\text{NO}_3)_2 \cdot 6\text{H}_2\text{O}$], lead [$\text{Pb}(\text{NO}_3)_2$], and zinc [$\text{Zn}(\text{NO}_3)_2 \cdot 6\text{H}_2\text{O}$] (Japanese Industrial Standard

special grade), as well as rhodamine B (RhB), ethanol (99.5%), hydrochloric acid (HCl), sodium hydroxide (NaOH) and 4,7,10-Trioxa-1,13-tridecanediamine (TTDDA) were purchased from Wako Pure Chemical Industries Ltd., Japan. Ultrapure water was obtained from a WR600G Autopure Ultraviolet Water Purification System (Yamato Scientific, Tokyo, Japan).

Experimental

CDs preparation

To prepare the TEMPO-CDs, ~ 5 g TEMPO-CNF aqueous dispersion was mixed with different volumes of TTDDA (0.1, 0.2, 0.3, 0.4, and 0.5 mL) in a beaker and placed in a domestic microwave oven (NE-S20, National, Japan), which was powered at 300, 500, and 700 W for periods of 1, 2, 3, 4, and 5 min. Subsequently, 20 mL of water was added to the beaker on a stirrer, to dissolve the TEMPO-CDs at room temperature for 1 h. After purification with a 0.22 µm syringe filter, TEMPO-CD aqueous solutions were obtained.

Similar processes were applied to the preparation of CNC-CDs and ACC-CDs by maintaining a constant NC content in the dispersion.

Characterization

Infrared spectra measurements (FTIR)

Fourier-transform infrared (FTIR) spectroscopy (FT/IR-6100, JASCO Corporation, Tokyo, Japan) was used to characterize the samples at wavenumbers of 500–4000 cm^{-1} at 25 °C. Solid NC and CD samples were stored in a desiccator to dry for 24 h; then, they were measured using a pellet containing the samples and KBr in a 1:100 mass ratio.

X-ray photoelectron spectroscopy (XPS)

The surface compositions of the NC and CD films were analyzed by X-ray photoelectron spectroscopy (XPS, JPS-9010TR, JEOL, Japan), using a $\text{MgK}\alpha$ (1253.6 eV) X-ray source operating at 100 W (10 kV, 10 mA).

X-ray diffractometry (XRD)

The dried solid TEMPO-CNF and TEMPO-CD samples were subjected to X-ray diffractometry (XRD, D8 Advanced, AXS-Bruker, Germany) to identify crystal structures in the 2θ range (10°–90°); the scans were conducted at a 2θ scan speed of 0.2°/s at 40 kV and 40 mA, using $\text{Cu-K}\alpha$ radiation (1.5418 Å).

Thermal study

To perform thermodynamic characterization, TEMPO-CNF and TEMPO-CD aqueous dispersions were dried at 50 °C in an oven for 24 h, to generate films. For thermogravimetric analysis (TGA), TEMPO-CNF and TEMPO-CDs were examined using a thermogravimetric analyzer (TG/DTA7300, Seiko Instruments Inc., Japan) and heated from 50 to 550 °C at a heating rate of 10 °C/min in an atmosphere of argon gas flowing at 200 mL/min. The differential scanning calorimetry (DSC, X-DSC7000, Seiko Instruments Inc., Japan) curve of TEMPO-CDs was determined during heating (50–550 °C) and cooling (550–50 °C) processes under the same atmosphere.

Morphological study

Transmission electron microscopy (TEM) (H-7650, Hitachi, Japan) was used to determine the particle diameter distribution of the TEMPO-CDs. After 300 s of ultrasonication using an ultrasonic homogenizer (UH-600S; SMT Co., Ltd., Tokyo, Japan), the samples were prepared by placing a drop of TEMPO-CD solution onto a carbon-coated formvar Cu grid and drying it with dry nitrogen (N_2) gas for ~ 10 min at 25 °C. Image J software was used to analyze the particle diameter.

Optical characterization of TEMPO-CDs

The ultraviolet–visible (UV–Vis) absorption spectra of TEMPO-CNF and TEMPO-CDs were acquired using a UV–Vis spectrophotometer (UV-3100PC, Shimadzu, Japan) at 25 °C.

The emission and excitation spectra of the TEMPO-CDs were recorded using a FL spectrophotometer (F-4600, Hitachi, Japan) at 25 °C.

The influence of pH of TEMPO-CD solution on the FL intensity was evaluated by adding different

amounts of HCl or NaOH aqueous solutions. All the pH values were determined through a pH meter (Laqua F-74, Horiba, Japan). The emission intensity values at 449 nm and 25 °C were recorded at an excitation wavelength of 390 nm.

Fluorescence quantum yield (QY) of TEMPO-CDs

The “quantum yield (QY)” is an important measure of photon-emission efficiency for fluorescent probes; it is often defined as the ratio between the numbers of photons emitted and absorbed in photochemical reactions (Li and Li 2017; Villamena 2017).

The QY can be expressed as a function of the radiative and nonradiative rates, as

$$Q = \frac{\text{Number of photons emitted}}{\text{Number of photons absorbed}} = \frac{k_r}{k_{nr} + k_r}, \quad (1)$$

where Q is the QY, k_r is the radiative rate, and k_{nr} is the nonradiative rate.

Absolute QY measurements require a complex and expensive arrangement to collect all the emitted photons, as well as several subsequent corrections (Balabhadra et al. 2017). In this study, the relative QY was measured according to an established procedure (employing a spectrofluorometer) as well as a comparative method (Lakowicz 2013), in which the RhB in an ethanol solution with 56% QY (Rurack and Spieles 2011) was chosen as a standard for the calculation, using

$$Q = Q_{RhB} \times \frac{A_{RhB}}{I_{RhB}} \times \frac{I}{A} \times \frac{\eta^2}{\eta_{RhB}^2}, \quad (2)$$

where Q is the QY, A is the absorption intensity, I is the integrated emission intensity, and n is the refractive index. The subscript “RhB” refers to the standard RhB for an ethanol solution. In this experiment, $\eta = 1.33$ and $\eta_{RhB} = 1.36$.

To minimize the effects of re-absorption on emission intensity (Arbela 1980), the A values of all samples were maintained below 0.10, as recorded.

Quenching effect between metal ions and TEMPO-CDs

Metal-nitrate salt solutions containing Ag^+ , Ca^{2+} , Cd^{2+} , Co^{2+} , Cu^{2+} , Fe^{3+} , K^+ , Mg^{2+} , Mn^{2+} , Na^+ , Ni^{2+} , Pb^{2+} , and Zn^{2+} at 80 ppm were prepared.

Subsequently, 0.9 mL aqueous solutions of these metal ions were added to a 0.9 mL TEMPO-CD solution, to obtain a final metal-ion concentration of 40 ppm.

The emission intensity at 449 nm was recorded at an excitation wavelength of 390 nm after 5, 60, 120, 240, 360, 480, and 600 s with a FL spectrophotometer at 25 °C. Each data point was obtained as the mean value over four measurements.

The interface-effect of other metal ions were further carried out by measuring the FL intensity of the mixtures of 80 ppm of Fe^{3+} (or Mn^{2+}) and 80 ppm of the above-mentioned other metal ions were added into the TEMPO-CDs solution, respectively.

Photographs were taken under UV irradiation, generated by a UV lamp (LUV-6, As One Corporation, Japan) at 365 nm, with a power of 6 W and a frequency of 50 Hz.

Detection of Fe^{3+} and Mn^{2+} ions

A TEMPO-CD aqueous solution was obtained under identical experimental conditions by adding 50 mL of ultrapure water to the dried yellow solid, followed by purification with a 0.22 μm syringe filter.

For the emission spectra, 0.9 mL Fe^{3+} or Mn^{2+} ion solutions at concentrations of 1, 2, 3, 4, 5, 10, 20, 25, 30, 40, 50, 60, 70, 80, 90, 100, 200, 300, 400 and 500 ppm were added to the 0.9 mL TEMPO-CDs suspensions.

The emission intensity values at 449 nm and 25 °C were recorded at an excitation wavelength of 390 nm after 5 s for Fe^{3+} and 10 min for Mn^{2+} .

Results and discussion

No NC species changed color after being treated solely by the microwave oven, and they all remained transparent (TEMPO-CNF and CNC) or white (ACC-CNF). When the microwave treatment was applied to a mixture of different species of NCs vs. TTDDA, the mixture turned dark yellow. The reaction speeds measured from the color change were ordered as TEMPO-CNF > CNC > ACC-CNF. Moreover, the color became deeper under an increase in reaction time and TTDDA volume, as shown in Fig. S1.

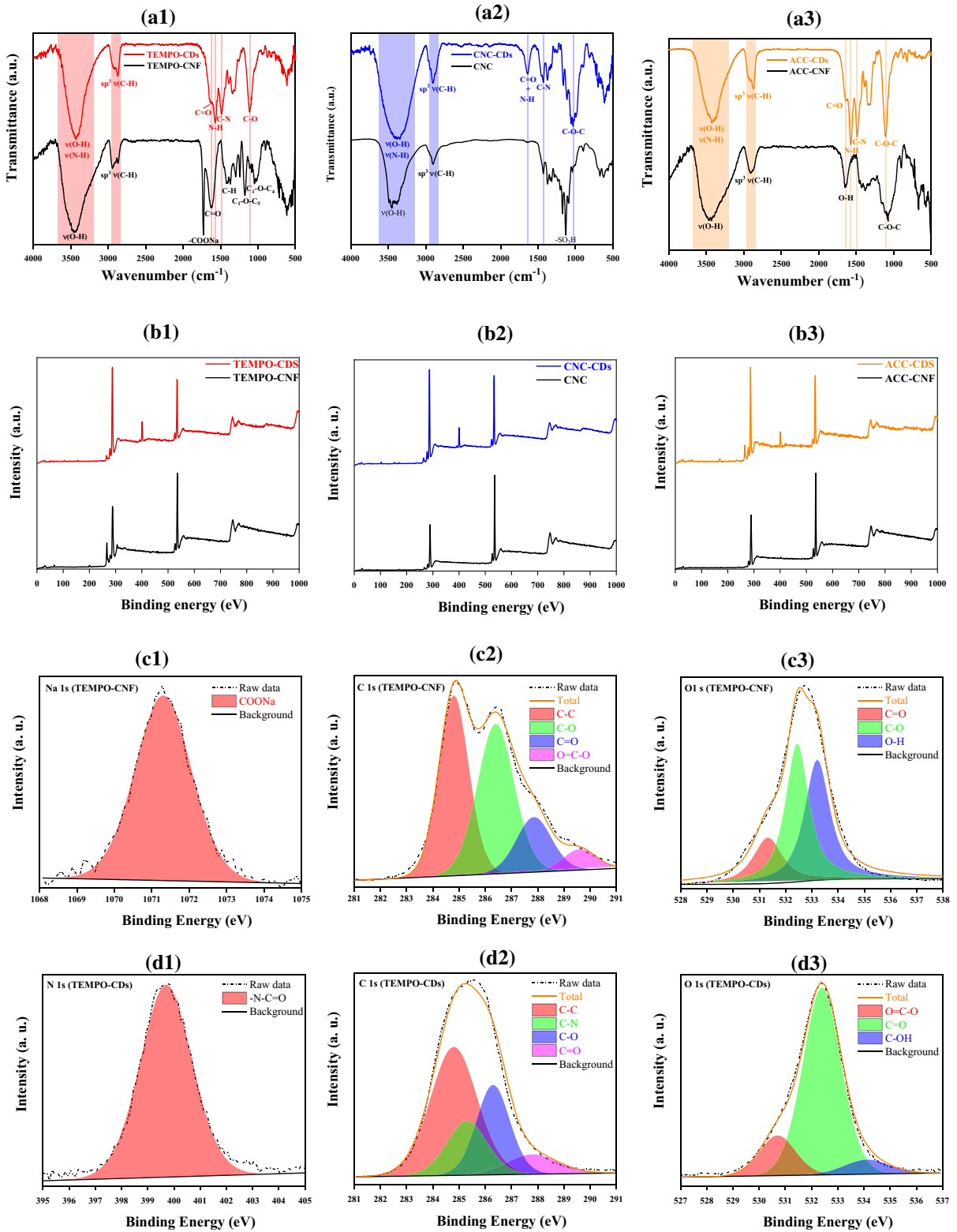


Fig. 1 (a1-3) FTIR and (b1-3) full scan XPS spectra of NCs and CDs, and high resolution XPS spectra of (c1) Na1s, (c2) C1s and (c3) O1s of TEMPO-CNF; and (d1) N1s, (d2) C1s and (d3) O1s of TEMPO-CDs

Table 1 Chemical composition of the NC and CDs films surface

Sample	C%	O%	N%	Na%	S%
TEMPO-CNF	72.71	26.57	NA	0.72	NA
TEMPO-CDs	74.75	14.77	10.48	NA	NA
CNC	65.65	33.63	NA	NA	0.81
CNC-CDs	72.32	19.49	8.19	NA	NA
ACC-CNF	69.31	30.69	NA	NA	NA
ACC-CDs	71.41	21.81	6.79	NA	NA

*NA: not available

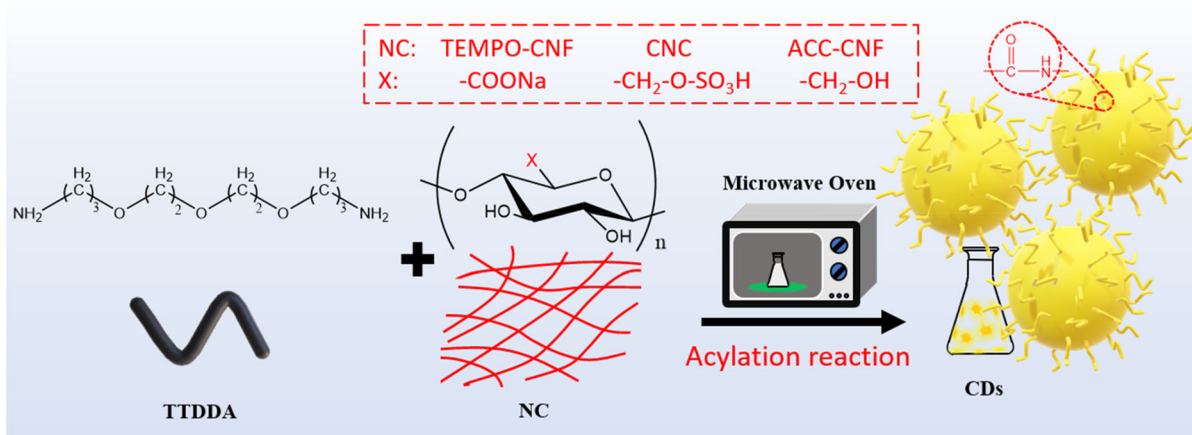
Characterization

Figure 1a1 shows the FTIR spectrum for TEMPO-CNF. The peaks at 1728 and 1620 cm^{-1} were assigned to the carboxylate ($-\text{COO}^-$) groups and carbonyl ($\text{C}=\text{O}$) stretching of sodium carboxylate ($-\text{COONa}$), respectively, at the C_6 position (Jiang et al. 2017). O–H stretching vibrations can be observed across a broad range of 3000–3650 cm^{-1} . The peaks at 2941 and 2869 cm^{-1} correspond to sp^3 C–H asymmetrical and symmetrical modes, respectively. The peaks for C–O–C groups can be found at 1172 and 1041 cm^{-1} , corresponding to $\text{C}_1\text{–O–C}_5$ and $\text{C}_1\text{–O–C}_4$, respectively (Poyraz et al. 2018).

For TEMPO-CDs, the bond between 3000 and 3650 cm^{-1} is still observable, but the peak shows a red-shift compared to the results for TEMPO-CNF. This can be regarded as a combination of O–H and N–H groups, where N–H is located at a lower wavenumber. The sp^3 C–H (2920 cm^{-1}) and C–H symmetrical (2869 cm^{-1}) stretching modes also exhibited a red-shift. The carbonyl ($\text{C}=\text{O}$) peak was observed at 1623 cm^{-1} . The peak at 1572 cm^{-1} corresponds to N–H deformation in the $-\text{CONH}-$ groups (Roy et al. 2016; Yang et al. 2014). No peak was observed for the $\text{C}_1\text{–O–C}_4$ and $\text{C}_1\text{–O–C}_5$ groups, though a strong C–O stretching peak was identified at 1110 cm^{-1} .

Regardless of the similarity between the FTIR spectra of the three types of NCs, Fig. 1a2 shows the unique $-\text{O–SO}_3\text{H}$ peak for CNC at 1169 cm^{-1} ; meanwhile, Fig. 1a3 shows no unique peak for ACC-CNF but a typical cellulose spectrum, because ACC-CNF is mechanically prepared from microcrystalline wood cellulose via aqueous counter collision. The FTIR spectra of both CNC-CDs [Fig. 1a2] and ACC-CDs [Fig. 1a] also exhibit N-related $-\text{CONH}$ peaks as TEMPO-CDs.

The peak assignments in the FTIR spectra were further verified by XPS analysis, using all types of NCs and CDs. The chemical compositions of all sample surfaces are summarized in Table. 1. The relative elemental content of O visibly decreased after the reaction, whilst that of C increased slightly. Characteristically, N was observed in all CDs after microwave treatment followed by purification. TEMPO-CDs contained the highest proportion of N



Scheme 1 Schematic diagram of the mechanism of CDs synthesis

(10.48%), whereas ACC-CDs contained the smallest (6.79%). As shown in Fig. S1, this result may relate to the color-change condition and the efficiency of the chemical reaction described in the FTIR results. When the synthesized CDs were compared against their original NC materials, there is no Na signal on a TEMPO-CD surface and no S signal on a CNC-CD surface. This indicates that the C₆ position (–COONa in TEMPO-CNF, –O–SO₃H in CNC, and –OH in ACC-CNF) is involved in the reaction.

In the full-scan XPS spectrum (0–1000 eV) of TEMPO-CNF, two major peaks of C1s (285 eV) and O1s (532 eV) were identified, as shown in Fig. 1b; meanwhile, a small peak of Na1s was observed at ~ 1,072 eV, as shown in Fig. 1c). The result of the deconvolution treatment for the high-resolution C1s spectrum of TEMPO-CNF revealed four main peaks at 284.8 (C–C), 286.4 (C–O), 287.9 (C = O), and 289.6 eV (O = C–O) (Benkaddour et al. 2014; Nechporchuk 2015), as shown in Fig. 1c2. The high-resolution O1s spectrum presents three main peaks at 531.3 (C = O), 532.3 (C–O), and 533.2 eV (O–H), as shown in Fig. 1c3.

Figure 1b also shows three major peaks of C1s (286 eV), N1s (401 eV), and O1s (532 eV) in the full-scan XPS spectrum of TEMPO-CDs. In addition, no such peak related to Na1s was found, indicating that the TEMPO-CDs were fully purified. The high-resolution C1s spectrum confirmed the presence of four main peaks at 284.8 (C–C), 285.3 (C–N), 286.3 (C–O), and 287.9 eV (C = O), as shown in Fig. 1d1. The O1s high-resolution spectrum in Fig. 1d2 exhibits three main peaks located at 530.7 (O = C–O), 532.4 (C = O), and 534.1 eV (C–OH). Among them, the C = O peak at 532.4 eV should relate to –N–C = O groups, which corresponds to the 399.7 eV peak in the N1s high-resolution spectrum, as shown in Fig. 1d3.

Figure 1a2 depicts the full-scan XPS spectra of CNC and CNC-CDs, whereas Fig. 1a3 shows the full-scan XPS spectra of ACC-CNF and ACC-CDs. Similar to TEMPO-CDs, compared to the original NC materials, a new peak corresponding to –CONH– was identified in the high-resolution XPS spectra of the CNC-CDs (Fig. S2) and ACC-CDs (Fig. S3).

As discussed above, we conclude that –CONH– groups were synthesized through the acylation reaction between TTDDA and NCs, under microwave treatment, as illustrated in Scheme 1.

Figure 2a shows a TEM image of the synthesized TEMPO-CDs (average diameter: 7.86 nm). The lattice fringes distances in HR-TEM images in Fig. 2b can be identified to be 0.348, 0.242 and 0.218 nm, corresponding to the basal plane spacing (d_{200}), the in-plane constant and the in-plane lattice spacing (d_{1-00}). The lattice fringes condition is similar to Zheng et al. (2018) where they applied glucose as the resource, while cellulose is derived from D-glucose units jointed by β (1 \rightarrow 4)-glycosidic bonds. The TEMPO-CNF XRD pattern in Fig. 2c exhibits a cellulose I structure at 15.7° (1–10), 16.5° (110), 23.0° (200), and 35.0° (004), respectively (Khenblouche et al. 2019). TEMPO-CDs synthesized with 0.1 mL TTDDA featured an XRD pattern similar to that of TEMPO-CNF; however, the intensity of the cellulose I structure was lower because of the destruction of the TEMPO-CNF crystalline region. With 0.2 mL of TTDDA, the cellulose I structure was still weakly observed; however, three new peaks appeared at 22.4°, 29.5°, and 42.0°, presumably related to the C skeleton in TEMPO-CDs. However, TEMPO-CDs synthesized with 0.4 and 0.6 mL TTDDA exhibited only one peak at 22.4°, indicating that only disordered carbon atoms were retained in the product. The schematic diagram of crystalline change tendency is presented in Fig. 2d.

Following previous studies of CDs, Du et al. (2014) synthesized CDs from renewable waste products of bagasse; they reported two broad peaks centered at ~ 13.6° and 28.8° as indicating highly disordered carbon atoms, but they neglected the peak at ~ 42.0° in their study. Skowroński and Osińska (2014) performed a formaldehyde-based polycondensation of resorcinol to obtain CDs, and they treated the large and broad peaks at 23.6° and 44.1° as the (002) and (101) planes of the graphitic nanodomains, respectively, embedded in the matrix of disordered carbon. The CDs achieved by Edison et al. (2016) showed broad 2θ peaks at ~ 23.7° and 42.0°; these were assigned to disordered carbon atoms with sharp peaks in the (002) and (100) planes of the hexagonal graphite structure. Peng and Sejdic (2009) reported two peaks at ~ 24.0° (002) and 44.8° (100) as representing the crystalline structure signal of carbogenic nanoparticles for the sample, though the study neglected the small peak at ~ 29.8°. However, the CDs synthesized by ascorbic acid exhibited only one broad diffraction peak (centered at 25.0°), owing to the highly disordered carbon atoms (Gong et al. 2014).

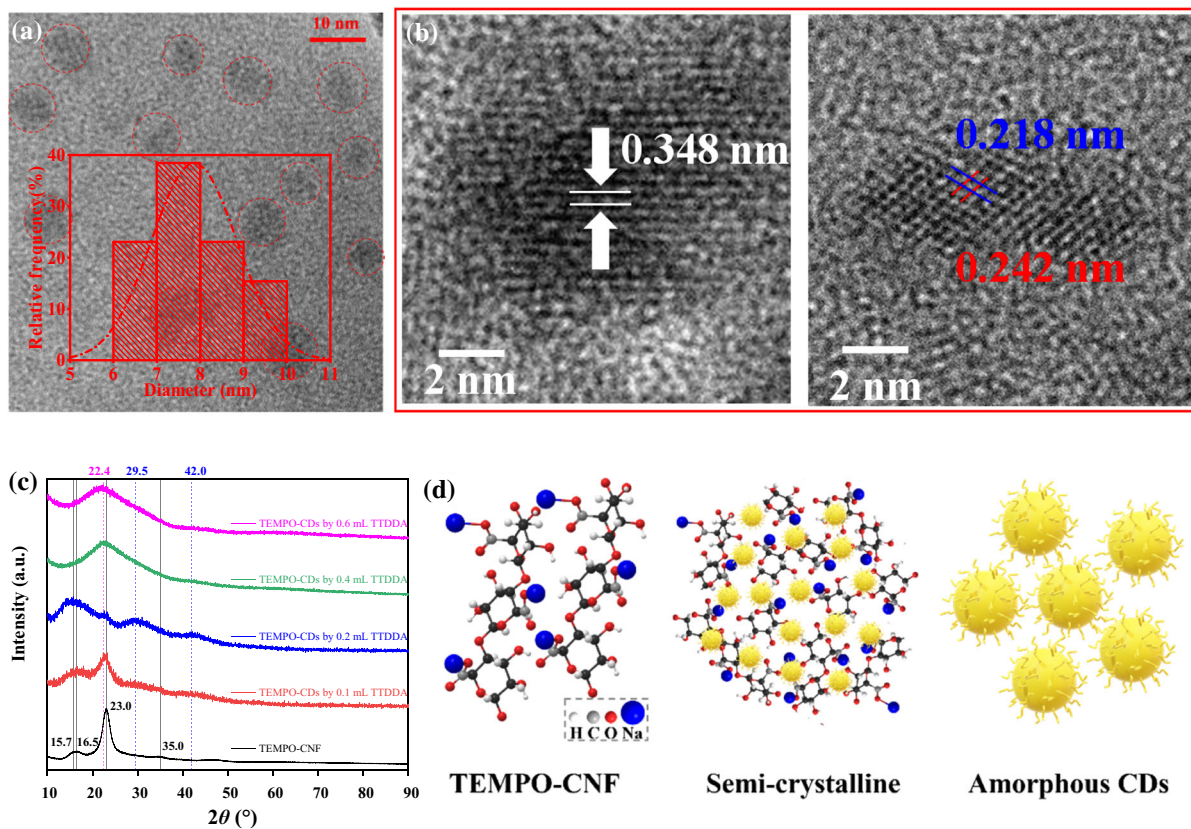


Fig. 2 **a** TEM image and histogram of particle size distribution for TEMPO-CDs produced with 0.4 mL TTDDA by 500 W microwave treatment for 3 min; **b** HR-TEM images of CDs; **c** XRD patterns of TEMPO-CNF and TEMPO-CDs synthesized

with different volumes of TTDDA by 500 W microwave treatment for 3 min, and **d** schematic diagrams of TEMPO-CNF, semi-crystalline and amorphous CDs

As mentioned above, all three peaks obtained after microwave treatment could be regarded as signals of the TEMPO-CDs. The mass ratio between TTDDA and TEMPO-CNF in the dispersion influences the crystalline state of the product. For the constant TEMPO-CNF dispersion mass applied in this study, TEMPO-CDs synthesized with smaller volumes of TTDDA were present in a semi-crystalline state as a combination of TEMPO-CDs and cellulose skeleton fragments in different degrees; meanwhile, TEMPO-CDs synthesized with larger volumes of TTDDA were present in an amorphous state, as shown in Fig. 2c. Meanwhile, the 5 g TEMPO-CD dispersion was converted into amorphous TEMPO-CDs only when the volume of TTDDA exceeded 0.4 mL.

As shown in Fig. 3, following free-moisture evaporation up to 100 °C, the bound water evaporated at ~ 120 °C (Jiang et al. 2016; Kumar et al. 2014) in

both TEMPO-CNF and TEMPO-CD thermogravimetric (TG) curves.

It is generally accepted that the thermal decomposition of cellulosic materials occurs in the temperature range of 200–400 °C (Meng et al. 2014); this range can be divided into two periods (Barnes et al. 2019; Fukuzumi et al. 2010):

(1) Dehydration along the cellulose chain: occasional chain scission that leaves the main β -1,4-polysaccharide skeleton unchanged.

(2) Pyrolytic fragmentation: generation of aromatized entities during fragmentation and formation of a highly cross-linked carbon skeleton.

For TEMPO-CNF, a multistep degradation process is involved in thermal degradation, as shown in Fig. 3a. The decomposition of TEMPO-CNF began at ~ 206 °C, as indicated by the TG curve. In the derivative TG (DTG) curve, two main peaks were observed at 239 and 293 °C, near to those reported in

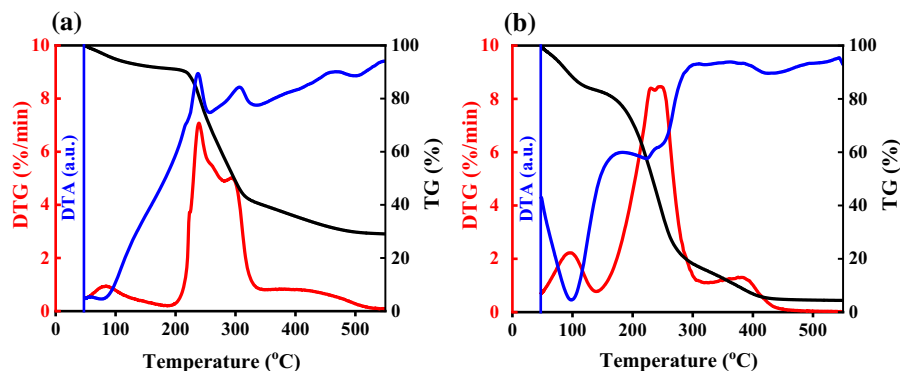


Fig. 3 TG/DTG/DTA curves of **a** TEMPO-CNF and **b** TEMPO-CDs synthesized by 500 W microwave treatment for 3 min

previous studies [233 and 282 °C (Fukuzumi et al. 2010) and 224 and 272 °C (Meng et al. 2014), both under N₂ gas flow]. Two main related peaks also appeared as two clear exothermic peaks in the DTA curve. The thermal decomposition (T_d) point at ~239 °C exhibits a 7.1 wt%/min maximum in the DTG curve, which arises from the decarboxylation of –COONa groups; meanwhile, the DTG peak at 293 °C (5.0 wt%/min) is related to the crystalline cellulose chains.

For the TEMPO-CDs, the TG curve showed a distinct mass loss in the temperature range of 150–310 °C, with only one T_d point observed in the DTG curve at ~250 °C (8.4 wt%/min) in Fig. 3b; this differs from the case of TEMPO-CNF. In the same temperature window as the DSC curve shown in Fig. S4, the endothermic peak at 70 °C (-7.11 mV) was due to the evaporation of water, whereas the endothermic peak at 213 °C (3.99 mV) was attributed to the decomposition of C=O- and C–O-related groups.

The lower thermal instability of TEMPO-CDs is mainly attributed to the ratio between the amorphous component and the total C substances after microwave treatment. The TG% leveled off after the reaction at ~550 °C and became 28.7% for TEMPO-CNF, 4.3% for 3-min treated TEMPO-CDs, and 2.4% for 5-min treated TEMPO-CDs (Fig. S5). This indicates fragmentation of the molecules. Regardless of the microwave treatment time, the weight loss progressed similarly. However, the residue of TEMPO-CDs decreased slightly with respect to microwave treatment time.

As for the optical properties, the inset in Fig. 4a shows that the TEMPO-CD product appears yellow under daylight irradiation but blue under 365 nm UV irradiation.

The optical gap corresponds to the energy gaps of the electronic transitions via absorption or emission of a single photon (Lakowicz 2013; Bredas 2014). The energy gap based on the optical gap between the two energy states during the transition was calculated using the Plank equation (Yu et al. 2018a), as

$$\Delta E = hv = \frac{hc}{e\lambda} = \frac{1240.82}{\lambda}, \quad (3)$$

where ΔE is the photon energy band (unit: eV), h is the Planck constant (6.626×10^{-34} J·s), e is the elementary charge (1.0602×10^{-19} C), ν is the photon frequency, c is the speed of light in vacuum (3×10^8 m·s⁻¹), and λ is the wavelength (units: nm).

In the UV-Vis spectra, the absorption peaks of TEMPO-CNF and TEMPO-CDs were completely different, indicating that TEMPO-CDs were synthesized via the microwave method and imbued with a functional moiety emitting FL. For TEMPO-CDs, the absorption peaks at 298 nm (4.16 eV) corresponded to the $\pi \rightarrow \pi^*$ transition of the sp² hybrid orbitals, and the peak at 330 nm (3.76 eV) corresponded to n $\rightarrow \pi^*$ transitions of the sp³ hybrid orbitals. Figure 4b shows that the TEMPO-CDs exhibit excitation-dependent emissions. When the excitation wavelength was increased from 360 to 500 nm, the emission peak was red-shifted from 443 (2.80 eV) to 531 nm (2.34 eV), displaying a color change from blue to green. The optimal combination of excitation and emission wavelengths featured maximum intensities

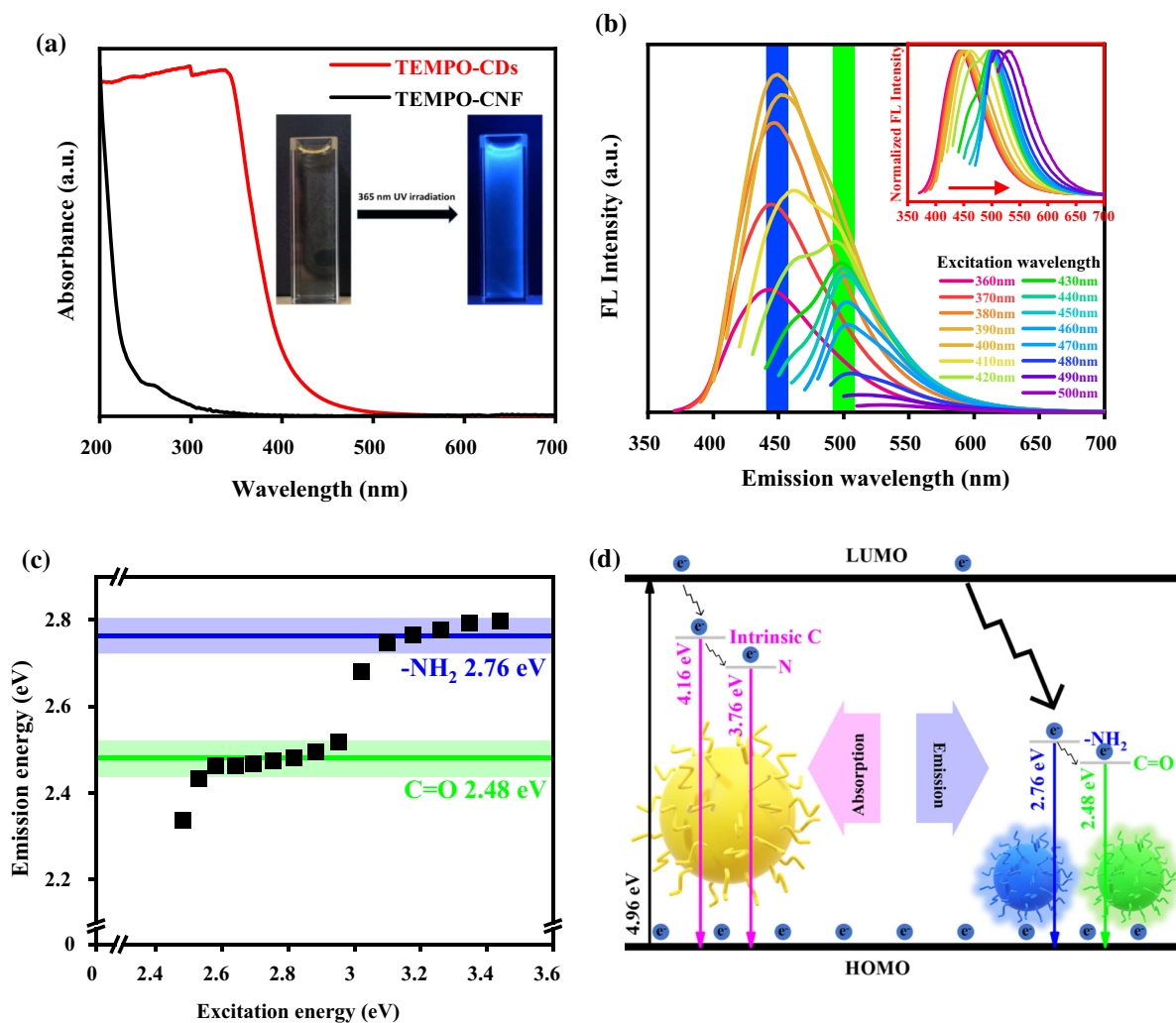


Fig. 4 **a** UV–Vis absorption spectra of TEMPO-CNF and TEMPO-CDs with photos of the CDs under sunlight (left) and 365 nm UV irradiations (right) inserted; **b** FL emission spectra of TEMPO-CDs at different excitation wavelengths with the

of 390 (3.18 eV) and 449 nm (2.76 eV) (bright blue ray), respectively.

Figure 4c shows the relationship between the energy of the FL emission peak (E_{em}) and excitation energy (E_{ex}). At values of E_{ex} below 2.6 eV and within the range 3.0–3.1 eV, E_{em} exhibited rapid increases. Meanwhile, two relatively steady energy ranges were observed in the results.

The measured band gap overlapped with a trace interference from the O and N elements and their related chemical moieties, producing a deviation in the excitation and emission spectra of TEMPO-CDs. The TEMPO-CDs exhibited two emission bands centered

normalized PL intensity spectra inserted; **c** relationship between the emission energy and the excitation energy, and **d** schematic of energy band structure and possible luminescence process for TEMPO-CDs

at 449 nm and 500 nm; these were correlated with the electron transition at the amino N- (2.76 eV) and C = O- (2.48 eV) related levels, respectively.

Based on the FTIR, XPS, UV–Vis, and FL spectra for TEMPO-CDs, as along with the band gap computational results, an energy band structure scheme for TEMPO-CDs was proposed based on the highest occupied–lowest unoccupied molecular orbitals (HOMO–LUMO) gap theory, as shown in Fig. 4d.

Zheng et al. (2017) also examined the relationship between E_{em} and E_{ex} , and they reported a fluorescent energy emission of 2.99 eV from the O-related energy band. However, the entire scale of E_{ex} involved in their

study ranged from ~ 2.7 to 4.4 eV, whereas the N-related energy band was not involved (< 2.70 eV). Yu et al. (2018a) explained the FL mechanism of CDs using the HOMO–LUMO gap theory and obtained a very similar energy band value to that obtained in this study (within 0.1 eV difference).

The excitation-dependent emission behavior of TEMPO-CDs related to the distribution of different surface states. In addition, the O and N elements and their related chemical moieties produced a trace error in the band gap, which produced deviations in the excitation and emission spectra of TEMPO-CDs.

Figure 5a shows that the QY increased under an increase in microwave treatment time (horizontally) and power strength (longitudinally). Figure 5b indicates that QY tended to increase under an increase in the volume of TTDDA (0.1, 0.2, 0.3, 0.4, and 0.5 mL) applied to synthesize TEMPO-CDs.

Above all, the QY tended to change rapidly during the initial stage with respect to the levels of the three aforementioned parameters: TTDDA volume, microwave time, and microwave power. However, the QY approached $\sim 17.76\%$, which may have been the upper limit of the QY under this method for 5 g TEMPO-CNF. In addition, the increasing QY trend also demonstrates the crystal structure transition obtained in the XRD results of TEMPO-CDs synthesized with different TTDDA volumes.

The pH value of the synthesized TEMPO-CD solution was approx. 9.3. The effect of the pH of

TEMPO-CD solutions on the FL is exhibited in Fig. 5c. Only one point (pH = 1) shows a relatively low FL value, which is likely to result from the protonation of $-\text{CONH}$ groups on a TEMPO-CD surface. However, the FL values exhibited a plateau in the pH region from 2 to 14. This makes TEMPO-CDs an excellent fluorescent probe candidate for most pH-value water environments unless under an extremely acidic environment (pH < 2).

Quenching effect between metal ions and TEMPO-CDs and its application to Fe^{3+} and Mn^{2+} detection

The emission spectra of the TEMPO-CDs under 390 nm excitation with different metal ions after 5 s were recorded at 449 nm, as shown in Fig. 6a. The FL intensity of all metal ions remained relatively constant, except in the case of Fe^{3+} ions. The FL intensity ratio (F/F_0) was evaluated as the quenching effect of the metal ions. F and F_0 denote the FL intensities of TEMPO-CDs at 449 nm in the absence and presence of metal ions, respectively. Figure 6b shows the differences in F/F_0 of the TEMPO-CD solutions in the presence and absence of various metal ions after 5 s. The figure shows that the F/F_0 ratio of the Fe^{3+} mixture was lowest, and other metal ions (except Mn^{2+}) exhibited marginal changes in FL intensity, which indicates that only Fe^{3+} had a considerable quenching effect on the FL of TEMPO-CDs. This

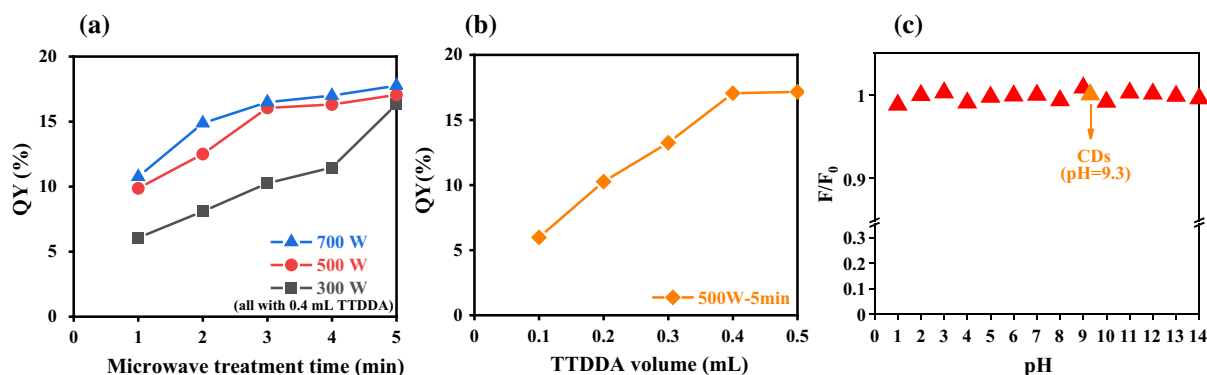


Fig. 5 The QY of TEMPO-CDs (a) synthesized from 0.4 mL TTDDA and 5 g TEMPO-CNF at different power levels and for different periods of microwave treatment time and (b) from

different volume of TTDDA and 5 g TEMPO-CNF at 500 W for 5 min; and (c) the effect of pH values on the FL intensity of TEMPO-CDs

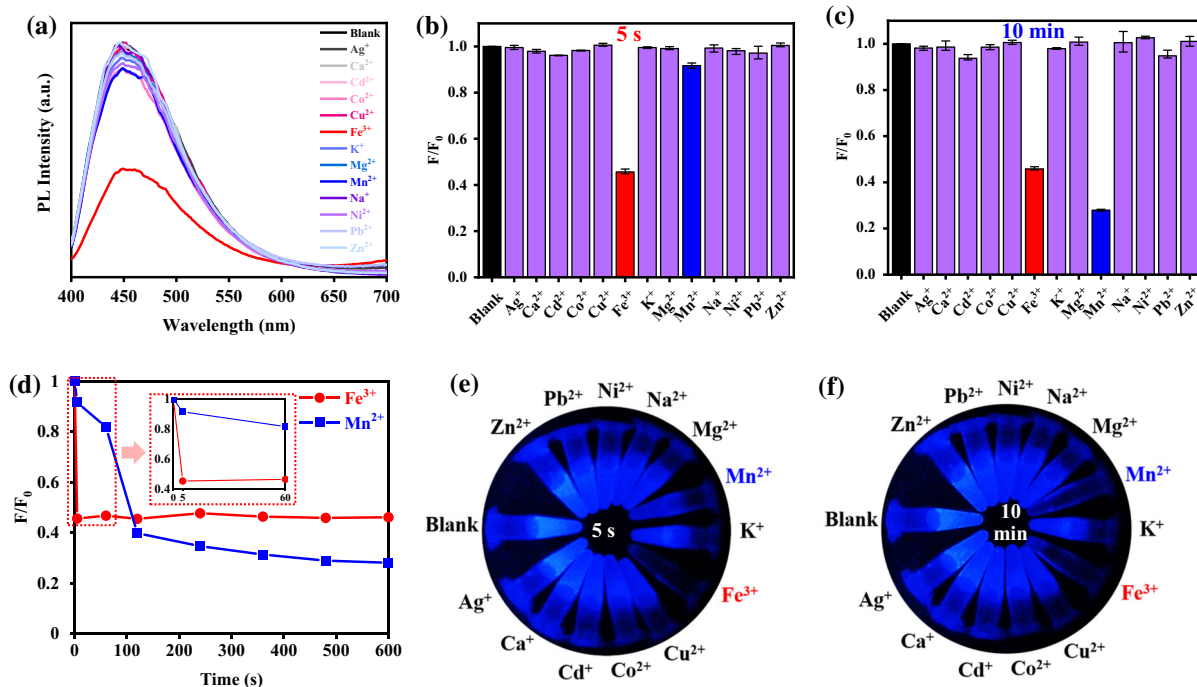


Fig. 6 a Emission spectra and F/F_0 of CDs solution mixed with various metal ion solutions at 40 ppm measured b 5 s and c 10 min after mixture, c F/F_0 of the mixture of CDs and 40 ppm

suggests that the synthesized TEMPO-CDs were able to detect Fe^{3+} ions within seconds via luminescence measurements.

However, as shown in Fig. 6c and d, the F/F_0 of the Mn^{2+} mixture decreased significantly over time; meanwhile, that of the Fe^{3+} and other metal ions (Fig. S6) remained similar to the results at 5 s. The F/F_0 ratio of Mn^{2+} continued to decrease for more than 10 min after mixing and became even smaller than that of Fe^{3+} . Meanwhile, after mixing Mn^{2+} and TEMPO-CDs, the color of the solution gradually became deep brown, as shown in Fig. S7. Photographs of TEMPO-CD dispersions containing 100 ppm of various metal ions, obtained under a 365 nm UV lamp for (a) 5 s and (b) 10 min, are presented in Fig. 6e and f. The results indicate that Mn^{2+} ions could also have a quenching effect on the CD solution, though at a lower speed than Fe^{3+} ions.

In terms of the valence electrons of Fe^{3+} and Mn^{2+} , both are arranged as $1s^2 2s^2 2p^6 3s^2 3p^6 4s^0 3d^5$, where the five d-orbitals are half-filled (Fig. S8). Fe^{3+} and Mn^{2+} ions could be absorbed on the surface of TEMPO-CDs, coordinate with the functional groups (N–H- or C = O-containing groups) on TEMPO-CDs, and form

Fe^{3+} and Mn^{2+} solutions as a function of time.; Photographs of CDs solutions containing 100 ppm various metal ions under 365 nm UV lamp after e 5 s and f 10 min

complexes. Electrons of the complexes formed between each of the two ion species and TEMPO-CDs were easily transferred to the half-filled 3d orbitals of these two ions. Because of this coordination interaction, electrons in the excited state of TEMPO-CDs were transferred to the unfilled orbital of Fe^{3+} and Mn^{2+} , resulting in a quenching of the FL.

Figure 7a shows the F/F_0 values of CDs- Fe^{3+} with various kinds of other metal ions at 5 s, when the influence from the other co-existing metal ions was negligible. As for the CDs- Mn^{2+} with other metal ions at 10 min in Fig. 7b, the F/F_0 value of CDs- Mn^{2+} - Fe^{3+} slightly decreased while other groups kept similar values. The interface-effect results of other metal ions prove the excellent anti-interference performance of TEMPO-CDs for detecting Fe^{3+} at 5 s and Mn^{2+} at 10 min.

The influence of quenching on the FL emitted from TEMPO-CDs indicates that the as-prepared TEMPO-CDs are a promising fluorescent probe for Fe^{3+} and Mn^{2+} detection.

According to the F/F_0 ratios for the mixture of Fe^{3+} ions and CDs at 5 s [fitting curve: $y = \exp(0.00033x^2 - 0.02306x + 0.01987)$

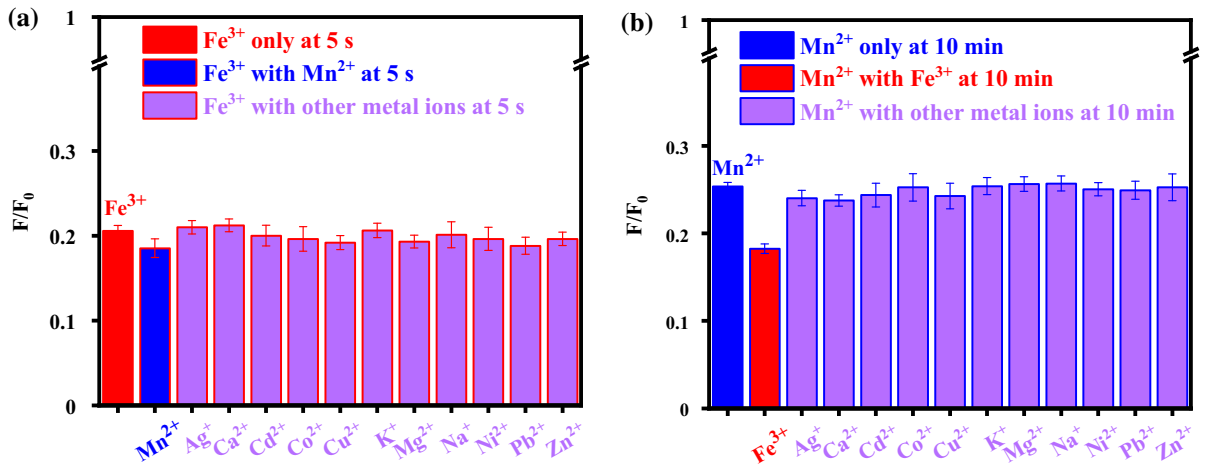


Fig. 7 a Selective FL response of CDs solution towards 80 ppm Fe³⁺, and interference of 80 ppm of other metal ions with 80 ppm Fe³⁺ at 5 s; and b selective FL response of CDs solution towards 80 ppm Mn²⁺, and interference of 80 ppm of other metal ions with 80 ppm Mn²⁺ at 10 min

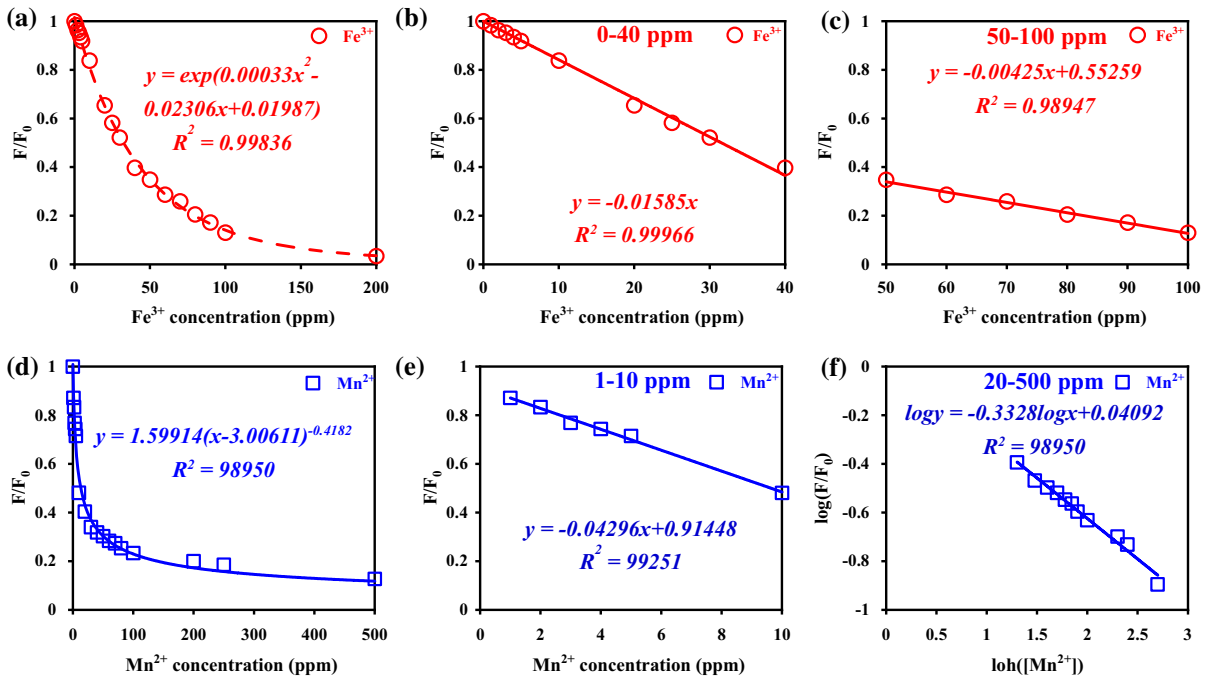
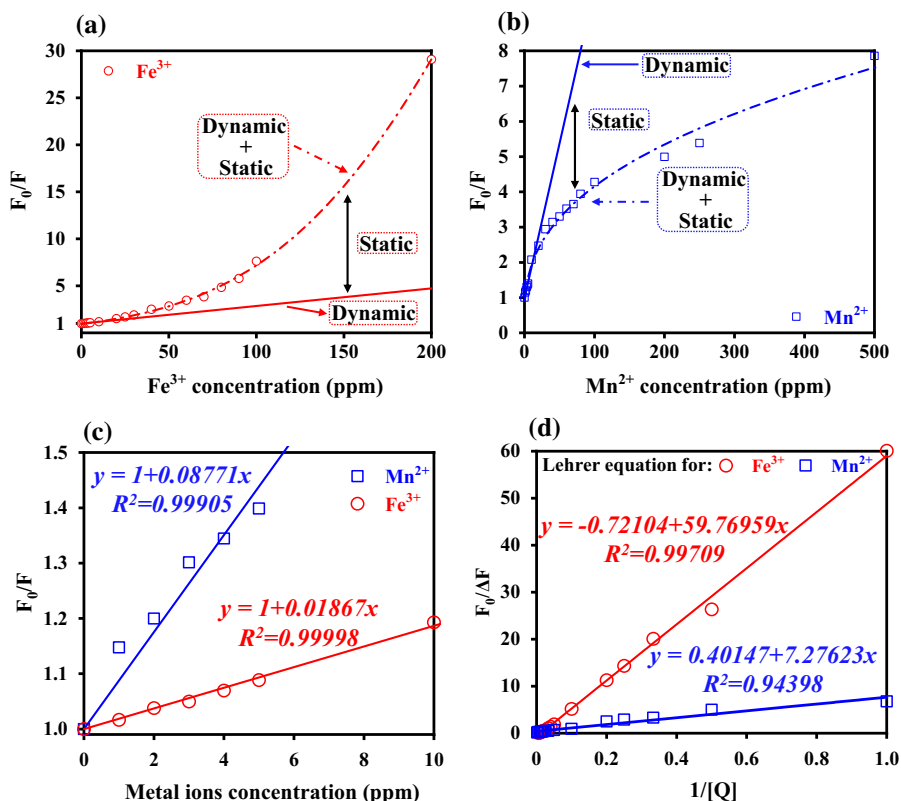


Fig. 8 Dependence of the F/F₀ value on the concentration of a Fe³⁺ ions (0–200 ppm) with b the linear relationship range of 0–40 ppm and c the linear relationship range of 50–100 ppm; and dependence of the F/F₀ value on the concentration of d Mn²⁺ ions (0–500 ppm) with e the linear relationship range of 1–10 ppm and f the log–log linear relationship range of 20–500 ppm

($R^2 = 0.99836$) presented in Fig. 8a, the F/F₀ value decreased under an increase in the concentration of Fe³⁺ ions.

However, the F/F₀ value of Fe³⁺ was unchanged when the Fe³⁺ concentration exceeded 200 ppm, which indicated that all the CDs were completely

Fig. 9 Fitting curves of the linear vs. nonlinear Stern–Volmer plots for (a) CDs- Fe^{3+} and (b) CDs- Mn^{2+} ; (c) detail fitting curves for linear Stern–Volmer plot for CDs- Fe^{3+} (0–5 ppm) and CDs- Mn^{2+} (0–10 ppm); and (d) Lehrer equation fitting curves for CDs- Fe^{3+} and CDs- Mn^{2+}



quenched by Fe^{3+} ions. Thus, 200 ppm should represent the upper limit for Fe^{3+} detection.

The F_0/F values for the Mn^{2+} ion and CD mixture after 10 min [fitting curve: $y = 1.59914(x - 3.00611)^{-0.4182}$ ($R^2 = 0.98950$)] also exhibited a decreasing tendency under an increase in the concentration of Mn^{2+} ions, as shown in Fig. 8d. Compared with the Fe^{3+} ions, the upper limit of the Mn^{2+} detection was much higher, reaching 500 ppm.

To simplify the detection formula, as well as to predict the Fe^{3+} and Mn^{2+} concentration in a more accurate level (especially for the low concentration range), favorable linear relationships were established for the two metal ions in different concentration ranges: (1) Fe^{3+} with two linear ranges at 0–40 ppm ($y = -0.01585x$, $R^2 = 0.99966$) in Fig. 8b and 50–100 ppm ($y = 0.00529 - 0.00425x$, $R^2 = 0.98947$) in Fig. 8c; and (2) Mn^{2+} with one linear range at 1–10 ppm ($y = 0.91448 - 0.04296x$, $R^2 = 0.99251$) in Fig. 8e and a log–log linear range at 20–500 ppm ($y = 0.04092 - 0.33280x$, $R^2 = 0.98950$) in Fig. 8f. For Fe^{3+} and Mn^{2+} ions, the TEMPO-CDs synthesized in this study exhibited a higher sensitivity

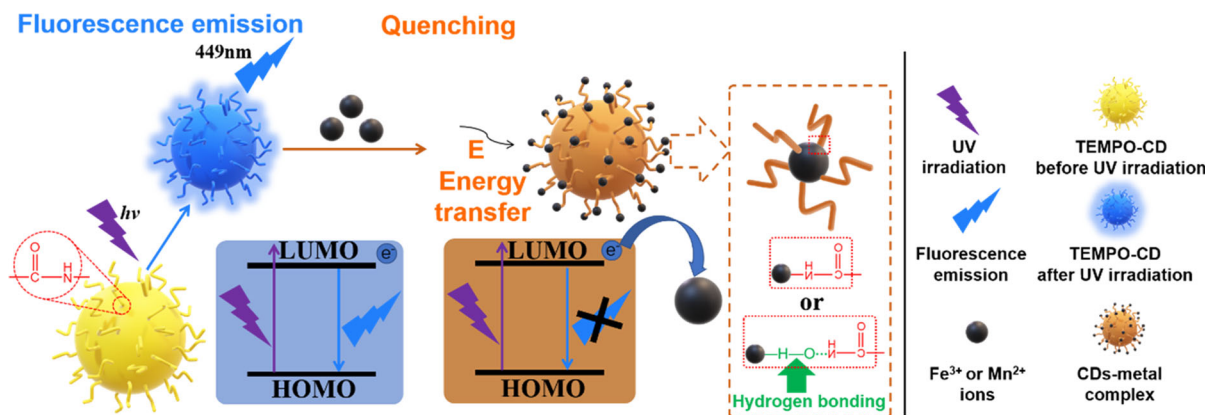
than other listed materials (e.g., metal nanoparticles) and nanosheets, as shown in Table S1–S2. Previous studies tested Fe^{3+} and Mn^{2+} in different testing systems; however, the current result indicates that Fe^{3+} and Mn^{2+} (with identical electron orbits) can be quenched by the same CD system for the first time.

To understand the fluorescence quenching of two kinds of metal ions, the following Stern–Volmer equation was used to for the analysis (Song et al. 2014):

$$F_0/F - 1 = K[M], \quad (4)$$

where K is the Stern–Volmer quenching constant; $[M]$ is the concentration of the quenchers (Fe^{3+} and Mn^{2+} in this study).

The relationships between F_0/F and $[M]$ of CDs- Fe^{3+} and CDs- Mn^{2+} are presented in Fig. 9a and b. The fitting data at low concentrations of both CDs- Fe^{3+} and CDs- Mn^{2+} groups follow the classical linear Stern–Volmer equation, implying only dynamic quenching at low metal concentration. A $K_{\text{Mn}^{2+}}$ value of 0.08771 indicates TEMPO-CDs has a higher detection sensitivity for Mn^{2+} than that of Fe^{3+}



Scheme 2 Fluorescence quenching mechanism schematic of TEMPO-CDs by Fe^{3+} and Mn^{2+}

($K_{\text{Fe}^{3+}} = 0.01867$), as shown in Fig. 9c. However, at high concentrations of both CDs- Fe^{3+} and CDs- Mn^{2+} , the deviation from linearity in Fig. 9a indicate that the initial condition described by the classical Stern–Volmer equation was not fulfilled. Under these circumstances, the modified Stern–Volmer equation (or Lehrer equation) is applied for the K calculation by introducing quenchable fraction of the fluorophores (α) (Leherer 1971):

$$\frac{F_0}{\Delta F} = \frac{F_0}{F_0 - F} = \frac{1}{\alpha} + \frac{1}{\alpha K[M]}, \quad (5)$$

where α lies between 0 and 1 ($0 \leq \alpha \leq 1$), representing the non-quenchable fluorophore.

Although both two F/F_0 values for CDs- Fe^{3+} and CDs- Mn^{2+} show a decreasing tendency in a downward curvature with the increasing metal ion concentrations (Fig. 8a, d), the curvatures for F_0/F in two groups are totally different (Fig. 9a and b).

The positive (upward) curvature in CDs- Fe^{3+} can be regarded as a combination of dynamic and static quenching as similar deviation can also be found in many other studies (Das et al. 2018). In this study, the static quenching possibly supposed to result from the formation of dark complex (Mátyus et al. 2006).

As for the CDs- Mn^{2+} , a negative (downward) curvature can be found in the result presumably because of (1) co-existence of fluorophores with different accessibilities to the quencher, or (2) a reverse reaction in the photochemical process (Naik et al. 2010; Geethanjali et al. 2015), although fewer studies for negative deviation results have been reported in the literature. In this study, the second

cause should be reasonable since hydrogen bond complexes were formed with fluorophore.

Above all, the schematic mechanisms of a fluorescence quenching mechanism schematic of TEMPO-CDs by Fe^{3+} and Mn^{2+} is illustrated in Scheme 2.

Conclusion

A simple, one-step, microwave-assisted synthesis approach for preparing CDs using various NCs and TTDDA was reported. TEMPO-CNF exhibited a higher conversion efficiency than ACC-CNF and CNC, as demonstrated by FTIR, XPS, and color change analyses.

The TEMPO-CDs prepared from 5 g TEMPO-CNF with 0.4 mL TTDDA exhibited an average diameter of 7.86 nm and produced excitation-dependent emissions with maximum intensities at excitation and emission wavelengths of 390 nm and 449 nm (bright blue ray), respectively. This wavelength dependency was theoretically explained by the HOMO–LUMO gap theory, based on energy band calculations in which C and N element states were assumed to have a sizeable influence.

The FL of the synthesized CDs was selectively and successfully quenched by Fe^{3+} and Mn^{2+} within seconds and after 10 min, respectively. Electrons in the complexes formed between each of the two ion species and TEMPO-CDs were easily transferred to the same half-filled 3d orbits of these two species of ions.

The quenching phenomenon was further applied to develop a fluorescent sensor that detects Fe^{3+}

(0–200 ppm) and Mn^{2+} (0–500 ppm) via mathematical curve fitting. This is a novel finding, from a viewpoint in that the use of a CD-related sensing system to detect Fe^{3+} and Mn^{2+} via the same CD probe has never been reported in the literature.

The further analysis for quenching effect was put forward based on classical Stern–Volmer and Lehrer models.

Acknowledgments The authors would like to thank the Open Facility Center for Science and Technology, University of Tsukuba, for allowing us to use their facilities; Nippon Paper Industries Co., Ltd., Japan, for providing TEMPO-CNF; and Chuetsu Pulp & Paper Co., Ltd., Japan, for providing ACC-CNF.

Author contributions Conceptualization: DH, TE; Methodology: DH, TE; Formal analysis and investigation: DH, K-HL, YX; Writing—original draft preparation: DH; Writing—review and editing: MK, MAN, KO, T; Funding acquisition: TE; Resources: MK, TE; Supervision: MK, MAN, KO, TE.

Funding This work was supported by the Japanese Society of Printing Science and Technology (JSPST) Printing Technology Granted Research Fund (2018), JSPS KAKENHI Grant Number 17KT0069, and the operating budget of the University of Tsukuba (for language editing).

Declarations

Conflicts of interest The authors declare that they have no conflicts of interest.

Ethics approval This article does not contain any studies with human participants or animals performed by any of the authors.

References

- Arbela IL (1980) Fluorescence quantum yield evaluation: corrections for re-absorption and re-emission. *J Photochem and Photobiol* 14:97–105. [https://doi.org/10.1016/0047-2670\(80\)80001-3](https://doi.org/10.1016/0047-2670(80)80001-3)
- Baker SN, Baker GA (2010) Luminescent carbon nanodots: emergent nanolights. *Angew Chem Int Ed* 49:6726–6744. <https://doi.org/10.1002/anie.200906623>
- Balabhadra S, Debasu ML, Brites CDS et al (2017) A cost-effective quantum yield measurement setup for upconverting nanoparticles. *J Lumin* 189:64–70. <https://doi.org/10.1016/j.jlumin.2017.03.054>
- Barnes E, Jefcoat JA, Albert EM et al (2019) Effect of cellulose nanofibrils and TEMPO-mediated oxidized cellulose nanofibrils on the physical and mechanical properties of poly(vinylidene fluoride)/cellulose nanofibril composites. *Polymers* 11:1091. <https://doi.org/10.3390/polym11071091>
- Benkaddour A, Journoux-Lapp C, Jradi K et al (2014) Study of the hydrophobization of TEMPO-oxidized cellulose gel through two routes: amidation and esterification process. *J Mater Sci* 49:2832–2843. <https://doi.org/10.1007/s10853-013-7989-y>
- Bredas JL (2014) Mind the gap! *Mater Horiz* 1:17–19. <https://doi.org/10.1039/C3MH00098B>
- Chowdhury S, Roj B, Dutta A, Mandal U (2018) Review on recent advances in metal ions sensing using different fluorescent probes. *J Fluoresc* 28:999–1021. <https://doi.org/10.1007/s10895-018-2263-y>
- Das R, Rajender G, Giri PK (2018) Anomalous fluorescence enhancement and fluorescence quenching of graphene quantum dots by single walled carbon nanotubes. *Phys Chem Chem Phys* 20:4527–4537. <https://doi.org/10.1039/C7CP06994D>
- De Acha N, Elosua C, Corres JM, Arregui FJ (2019) Fluorescent sensors for the detection of heavy metal ions in aqueous media. *Sensors* 19:599. <https://doi.org/10.3390/s19030599>
- Du F, Zhang M, Li X et al (2014) Economical and green synthesis of bagasse-derived fluorescent carbon dots for biomedical applications. *Nanotechnology* 25:315702. <https://doi.org/10.1088/0957-4484/25/31/315702>
- Duruibe JO, Ogwuegbu MOC, Ekwurugwu JN (2007) Heavy metal pollution and human biotoxic effects. *Int J Phys Sci* 2:112–118. <https://doi.org/10.5897/IJPS.9000289>
- Edison TN, Atchudan R, Sethuraman MG et al (2016) Microwave assisted green synthesis of fluorescent N-doped carbon dots: Cytotoxicity and bio-imaging applications. *J Photochem Photobiol B Biol* 161:154–161. <https://doi.org/10.1016/j.jphotobiol.2016.05.017>
- Emerit J, Beaumont C, Trivin F (2001) Iron metabolism, free radicals, and oxidative injury. *Biomed Pharmacother* 55:333–339. [https://doi.org/10.1016/S0753-3322\(01\)00068-3](https://doi.org/10.1016/S0753-3322(01)00068-3)
- Fukuzumi H, Saito T, Okita Y, Isogai A (2010) Thermal stabilization of TEMPO-oxidized cellulose. *Polym Degrad Stab* 95:1502–1508. <https://doi.org/10.1016/j.polyimdegradstab.2010.06.015>
- Fukuzumi H, Tanaka R, Saito T, Isogai A (2014) Dispersion stability and aggregation behavior of TEMPO-oxidized cellulose nanofibrils in water as a function of salt addition. *Cellulose* 21:1553–1559. <https://doi.org/10.1007/s10570-014-0180-z>
- Geethanjali HS, Nagaraja D, Melavanki RM, Kusanur RA (2015) Fluorescence quenching of boronic acid derivatives by aniline in alcohols—A Negative deviation from Stern–Volmer equation. *J Lumin* 167:216–221. <https://doi.org/10.1016/j.jlumin.2015.06.040>
- Golmohammadi H, Morales-Narváez E, Naghdi T, Merkoçi A (2017) Nanocellulose in sensing and biosensing. *Chem Mater* 29:5426–5446. <https://doi.org/10.1021/acs.chemmater.7b01170>
- Gong J, An X, Yan X (2014) A novel rapid and green synthesis of highly luminescent carbon dots with good biocompatibility for cell imaging. *New J Chem* 38:1376–1379. <https://doi.org/10.1039/c3nj01320k>

- Han FX, Banin A, Su Y et al (2002) Industrial age anthropogenic inputs of heavy metals into the pedosphere. *Sci Nat* 89:497–504. <https://doi.org/10.1007/s00114-002-0373-4>
- Hoeng F, Denneulin A, Bras J (2016) Use of nanocellulose in printed electronics: a review. *Nanoscale* 8:13131–13154. <https://doi.org/10.1039/c6nr03054h>
- Hou J, Zhang F, Yan X et al (2015) Sensitive detection of biothiols and histidine based on the recovered fluorescence of the carbon quantum dots-Hg(II) system. *Anal Chim Acta* 859:72–78. <https://doi.org/10.1016/j.aca.2014.12.021>
- Hu C, Yu C, Li M et al (2014) Chemically tailoring coal to fluorescent carbon dots with tuned size and their capacity for Cu(II) detection. *Small* 10:4926–4933. <https://doi.org/10.1002/smll.201401328>
- Hubbe MA, Ferrer A, Tyagi P et al (2017) Nanocellulose in thin films, coatings, and plies for packaging applications: a review. *BioResources* 12:2143–2233
- Jiang F, Dinh DM, Hsieh YL (2017) Adsorption and desorption of cationic malachite green dye on cellulose nanofibril aerogels. *Carbohydr Polym* 173:286–294. <https://doi.org/10.1016/j.carbpol.2017.05.097>
- Jiang Y, Zhao Y, Feng X et al (2016) TEMPO-mediated oxidized nanocellulose incorporating with its derivatives of carbon dots for luminescent hybrid films. *RSC Adv* 6:6504–6510. <https://doi.org/10.1039/c5ra17242j>
- Jorfi M, Foster EJ (2015) Recent advances in nanocellulose for biomedical applications. *J Appl Polym Sci* 132:41719–41738. <https://doi.org/10.1002/app.41719>
- Kawamura R, Ikuta H, Fukuzumi S et al (1941) Intoxication by manganese in well water. *Kitasato Arch Exp Med* 18:145–169
- Khenblouche A, Bechki D, Gouamid M et al (2019) Extraction and characterization of cellulose microfibrils from Retama raetam stems. *Polímeros* 29:e2019011. <https://doi.org/10.1590/0104-1428.05218>
- Kim HJ, Kwon HJ, Jeon S et al (2015) Electrical and Optical Properties of Nanocellulose Films and Its Nanocomposites. In: *Handbook of polymer nanocomposites*, processing, performance and application. Springer Berlin Heidelberg, pp 395–432 doi:<https://doi.org/10.1007/978-3-642-45232-1>
- Kiran S, Misra RD (2015) Mechanism of intracellular detection of glucose through nonenzymatic and boronic acid functionalized carbon dots. *J Biomed Mater Res A* 103:2888–2897. <https://doi.org/10.1002/jbm.a.35421>
- Klemm D, Kramer F, Moritz S et al (2011) Nanocelluloses: a new family of nature-based materials. *Angew Chem Int Ed* 50:5438–5466. <https://doi.org/10.1002/anie.201001273>
- Kondakis XG, Makris N, Leotsinidis M et al (1989) Possible health effects of high manganese concentration in drinking water. *Arch Environ Occup Health* 44:175–178. <https://doi.org/10.1080/00039896.1989.9935883>
- Kumar A, Negi YS, Choudhary V, Bhardwaj NK (2014) Characterization of cellulose nanocrystals produced by acid-hydrolysis from sugarcane bagasse as agro-waste. *J Phys Chem Mater* 2:1–8. <https://doi.org/10.12691/jmpc-2-1-1>
- Lakowicz JR (2013) *Principles of fluorescence spectroscopy*. Springer Science & Business Media, New York
- Lehrer SS (1971) Solute perturbation of protein fluorescence. Quenching of the tryptophyl fluorescence of model compounds and of lysozyme by iodide ion. *Biochem* 10:3254–3263. <https://doi.org/10.1021/bi00793a015>
- Li F, Liu C, Yang J et al (2014a) Mg/N double doping strategy to fabricate extremely high luminescent carbon dots for bioimaging. *RSC Adv* 4:3201–3205. <https://doi.org/10.1039/c3ra43826k>
- Li H, He X, Kang Z et al (2010) Water-soluble fluorescent carbon quantum dots and photocatalyst design. *Angew Chem Int Ed* 49:4430–4434. <https://doi.org/10.1002/anie.200906154>
- Li H, Zhu Y, Cao H et al (2013) Preparation and characterization of photocatalytic carbon dots-sensitized electrospun titania nanostructured fibers. *Mater Res Bull* 48:232–237. <https://doi.org/10.1016/j.materresbull.2012.10.052>
- Li J, Zuo G, Pan X et al (2018) Nitrogen-doped carbon dots as a fluorescent probe for the highly sensitive detection of Ag⁺ and cell imaging. *Luminescence* 33:243–248. <https://doi.org/10.1002/bio.3407>
- Li R, Li C (2017) Photocatalytic water splitting on semiconductor-based photocatalysts. In: *Advances in catalysis*, pp 1–57. doi:<https://doi.org/10.1016/bs.acat.2017.09.001>
- Li S, Li Y, Cao J et al (2014b) Sulfur-doped graphene quantum dots as a novel fluorescent probe for highly selective and sensitive detection of Fe³⁺. *Anal Chem* 86:10201–10207. <https://doi.org/10.1021/ac503183y>
- Li X, Wang H, Shimizu Y et al (2011) Preparation of carbon quantum dots with tunable photoluminescence by rapid laser passivation in ordinary organic solvents. *ChemComm* 47:932–934. <https://doi.org/10.1039/c0cc03552a>
- Liu C, Zhang P, Tian F et al (2011) One-step synthesis of surface passivated carbon nanodots by microwave assisted pyrolysis for enhanced multicolor photoluminescence and bioimaging. *J Mater Chem* 21:13163. <https://doi.org/10.1039/c1jm12744f>
- Liu R, Zhang J, Gao M et al (2015) A facile microwave-hydrothermal approach towards highly photoluminescent carbon dots from goose feathers. *RSC Adv* 5:4428–4433. <https://doi.org/10.1039/c4ra12077a>
- Malik LA, Bashir A, Qureshi A, Pandith AH (2019) Detection and removal of heavy metal ions: a review. *Environ Chem Lett* 17:1495–1521. <https://doi.org/10.1007/s10311-019-00891-z>
- Mátyus L, Szöllösi J, Jenei A (2006) Steady-state fluorescence quenching applications for studying protein structure and dynamics. *J Photochem Photobiol B* 83:223–236. <https://doi.org/10.1016/j.jphotobiol.2005.12.017>
- Meng Q, Li H, Fu S, Lucia LA (2014) The non-trivial role of native xylans on the preparation of TEMPO-oxidized cellulose nanofibrils. *React Func Polym* 85:142–150. <https://doi.org/10.1016/j.reactfunctpolym.2014.07.021>
- Naik AB, Naik LR, Kadadevarmath JS et al (2010) Fluorescence quenching of anthrylvinyl acetate by carbon tetrachloride. *J Photochem Photobiol A* 214:145–151. <https://doi.org/10.1016/j.jphotochem.2010.06.018>
- Cellulose nanofibers for the production of bionanocomposites. Dissertation, Université Grenoble Alpes
- Papanikolaou G, Pantopoulos K (2005) Iron metabolism and toxicity. *Toxicol Appl Pharmacol* 202:199–211. <https://doi.org/10.1016/j.taap.2004.06.021>
- Park SY, Lee HU, Park ES et al (2014) Photoluminescent green carbon nanodots from food-waste-derived sources: large-

- scale synthesis, properties, and biomedical applications. *ACS Applied Mater Interfaces* 6:3365–3370. <https://doi.org/10.1021/am500159p>
- Peng H, Travas-Sejdic J (2009) Simple aqueous solution route to luminescent carbogenic dots from carbohydrates. *Chem Mater* 21:5563–5565. <https://doi.org/10.1021/cm901593y>
- Peres TV, Schettinger MRC, Chen P et al (2016) Manganese-induced neurotoxicity: a review of its behavioral consequences and neuroprotective strategies. *BMC Pharmacol Toxicol*. <https://doi.org/10.1186/s40360-016-0099-0>
- Poyraz B, Tozluoğlu A, Candan Z et al (2018) TEMPO-treated CNF composites: pulp and matrix effect. *Fibers Polym* 19:195–204. <https://doi.org/10.1007/s12221-018-7673-y>
- Racetite BA (2014) Manganism in the 21st century: the Hanninen lecture. *Neurotoxicology* 45:201–207. <https://doi.org/10.1016/j.neuro.2013.09.007>
- Roy S, Das T, Zhang L, Hu XM (2016) Harnessing the maximum reinforcement of graphene oxide for poly(vinylidene fluoride) nanocomposites via polydopamine assisted novel surface modification. *RSC Adv* 6:69919–69929. <https://doi.org/10.1039/c6ra12997h>
- Rurack K, Spieles M (2011) Fluorescence quantum yields of a series of red and near-infrared dyes emitting at 600–1000 nm. *Anal Chem* 83:1232–1242. <https://doi.org/10.1021/ac101329h>
- Singh R, Gautam N, Mishra A, Gupta R (2011) Heavy metals and living systems: an overview. *Indian J Pharmacol* 43:246. <https://doi.org/10.4103/0253-7613.81505>
- Skowroński JM, Osińska M (2014) The influence of thermal treatment on the electrochemical properties of carbon–Ni–Pd composites. *J Solgel Sci Technol* 71:109–117. <https://doi.org/10.1007/s10971-014-3338-0>
- Song Y, Zhu S, Xiang S et al (2014) Investigation into the fluorescence quenching behaviors and applications of carbon dots. *Nanoscale* 6:4676–4682. <https://doi.org/10.1039/c4nr00029c>
- Sun X, Lei Y (2017) Fluorescent carbon dots and their sensing applications. *Trends Analyt Chem* 89:163–180. <https://doi.org/10.1016/j.trac.2017.02.001>
- Sun YP, Zhou B, Lin Y et al (2006) Quantum-sized carbon dots for bright and colorful photoluminescence. *J Am Chem Soc* 128:7756–7757. <https://doi.org/10.1021/ja062677d>
- Tang D, Liu J, Wu X et al (2014) Carbon quantum dot/NiFe layered double-hydroxide composite as a highly efficient electrocatalyst for water oxidation. *ACS Appl Mater Interfaces* 6:7918–7925. <https://doi.org/10.1021/am501256x>
- Villamena FA (2017) Fluorescence Technique. In: *Reactive species detection in biology*. pp 87–162. doi:<https://doi.org/10.1016/b978-0-12-420017-3.00003-7>
- Wang L, Cao HX, He YS et al (2019) Facile preparation of amino-carbon dots/gold nanoclusters FRET ratiometric fluorescent probe for sensing of Pb²⁺/Cu²⁺. *Sens Actuators B Chem* 282:78–84. <https://doi.org/10.1016/j.snb.2018.11.058>
- Wang W, Yang R, Li T et al (2020) Advances in recyclable and superior photocatalytic fibers: Material, construction, application and future perspective. *Compos B Eng* 205:108512. <https://doi.org/10.1016/j.compositesb.2020.108512>
- WHO (2003) *Iron in Drinking-water: Background document for development of WHO Guidelines for Drinking-water Quality*. Switzerland, Geneva
- WHO (2011) *Manganese in Drinking-water: Background document for development of WHO Guidelines for Drinking-water Quality*. WHO, Geneva, Switzerland
- Wu M, Wang Y, Wu W et al (2014) Preparation of functionalized water-soluble photoluminescent carbon quantum dots from petroleum coke. *Carbon* 78:480–489. <https://doi.org/10.1016/j.carbon.2014.07.029>
- Xiao L, Guo H, Wang S et al (2019) Carbon dots alleviate the toxicity of cadmium ions (Cd²⁺) toward wheat seedlings. *Environ Sci Nano* 6:1493–1506. <https://doi.org/10.1039/c9en00235a>
- Xu X, Ray R, Gu Y et al (2004) Electrophoretic analysis and purification of fluorescent single-walled carbon nanotube fragments. *J Am Chem Soc* 126:12736–12737. <https://doi.org/10.1021/ja040082h>
- Yang M, Tang Q, Meng Y et al (2018) Reversible “off-on” fluorescence of Zn²⁺-passivated carbon dots: mechanism and potential for the detection of EDTA and Zn²⁺. *Langmuir* 34:7767–7775. <https://doi.org/10.1021/acs.langmuir.8b00947>
- Yang MH, Yuan SS, Chung TW et al (2014) Characterization of silk fibroin modified surface: a proteomic view of cellular response proteins induced by biomaterials. *Biomed Res Int* 2014:209469. <https://doi.org/10.1155/2014/209469>
- Yoo D, Park Y, Cheon B, Park MH (2019) Carbon dots as an effective fluorescent sensing platform for metal ion detection. *Nanoscale Res Lett* 14:272. <https://doi.org/10.1186/s11671-019-3088-6>
- Yoshida K, Yamada T (1988) Long-period crystal lattices in thin Bi–Mn alloy films prepared by successive and simultaneous vacuum depositions. *Appl Surf Sci* 33:516–524. [https://doi.org/10.1016/0169-4332\(88\)90347-9](https://doi.org/10.1016/0169-4332(88)90347-9)
- Yu J, Liu C, Yuan K et al (2018a) Luminescence Mechanism of carbon dots by tailoring functional groups for sensing Fe³⁺ ions. *Nanomaterials*. <https://doi.org/10.3390/nano8040233>
- Yu L, Ren G, Tang M et al (2018b) Effective determination of Zn²⁺, Mn²⁺, and Cu²⁺ simultaneously by using dual-emissive carbon dots as colorimetric fluorescent probe. *Eur J Inorg Chem* 2018:3418–3426. <https://doi.org/10.1002/ejic.201800474>
- Zarjou A, Balla J, Balla G, Agarwal A (2011) Iron metabolism and oxidative stress. In: *Studies on renal disorders*. Springer, pp 205–228 doi:<https://doi.org/10.1007/978-1-60761-857-7>
- Zhang B, Liu C-y, Liu Y (2010) A novel one-step approach to synthesize fluorescent carbon nanoparticles. *Eur J Inorg Chem* 2010:4411–4414. <https://doi.org/10.1002/ejic.201000622>
- Zhang J, Chen X, Li Y et al (2018) A nitrogen doped carbon quantum dot-enhanced chemiluminescence method for the determination of Mn²⁺. *Anal Methods* 10:541–547. <https://doi.org/10.1039/c7ay02806g>
- Zheng B, Chen Y, Li P et al (2017) Ultrafast ammonia-driven, microwave-assisted synthesis of nitrogen-doped graphene quantum dots and their optical properties. *Nanophotonics* 6:259–267. <https://doi.org/10.1515/nanoph-2016-0102>
- Zhu W, Zhang J, Jiang Z et al (2014) High-quality carbon dots: synthesis, peroxidase-like activity and their application in

- the detection of H_2O_2 , Ag^+ and Fe^{3+} . RSC Adv 4:17387–17392. <https://doi.org/10.1039/c3ra47593j>
- Zhu H, Wang X, Li Y et al (2009) Microwave synthesis of fluorescent carbon nanoparticles with electrochemiluminescence properties. ChemComm 34:5118–5120. <https://doi.org/10.1039/b907612c>
- Zhuo K, Sun D, Xu P et al (2017) Green synthesis of sulfur- and nitrogen-co-doped carbon dots using ionic liquid as a precursor and their application in Hg^{2+} detection. J Lumin 187:227–234. <https://doi.org/10.1016/j.jlumin.2017.03.022>
- Zong J, Yang X, Trinchi A et al (2014) Carbon dots as fluorescent probes for “off-on” detection of Cu^{2+} and L-cysteine in aqueous solution. Biosens Bioelectron 51:330–335. <https://doi.org/10.1016/j.bios.2013.07.042>

Publisher’s Note Springer Nature remains neutral with regard to jurisdictional claims in published maps and institutional affiliations.